Dynamics of salt precipitation at pore scale during CO2 subsurface storage in saline aquifer

Yan, Lifei; Niftaliyev, Rustam; Voskov, Denis; Farajzadeh, Rouhi

DOI
10.1016/j.jcis.2024.08.265

Publication date
2025

Document Version
Final published version

Published in
Journal of Colloid and Interface Science

Citation (APA)
Yan, L., Niftaliyev, R., Voskov, D., & Farajzadeh, R. (2025). Dynamics of salt precipitation at pore scale during CO2 subsurface storage in saline aquifer. *Journal of Colloid and Interface Science*, *678*(Part B), 419-430. https://doi.org/10.1016/j.jcis.2024.08.265

Journal of Colloid and Interface Science 678 (2025) 419–430

Contents lists available at ScienceDirect

Journal of Colloid And Interface Science

journal homepage: www.elsevier.com/locate/jcis

Regular Article

Dynamics of salt precipitation at pore scale during CO_2 subsurface storage in saline aquifer

Lifei Yan [a,*], Rustam Niftaliyev [a,b], Denis Voskov [a,c], Rouhi Farajzadeh [a,d]

[a] Delft University of Technology, Department of Geoscience and Engineering, Stevinweg 1, 2628 CN Delft, the Netherlands
[b] Polytechnic University of Turin, Department of Environment, Corso Duca degli Abruzzi 24, 10129 Torino, TO, Italy
[c] Energy Science and Engineering, Stanford University, USA
[d] Shell Global Solutions International B.V., Grasweg 31, 1031 HW Amsterdam, the Netherlands

HIGHLIGHTS

- Impact of pore structure on salt precipitation is rigorously investigated.
- Important kinetic parameters of salt precipitation are derived from direct experimental observations.
- Impact of local heterogeneity and surface wettability on salt distribution is identified.
- Pore-scale backflow due to capillary gradient in porous media is observed.

GRAPHICAL ABSTRACT

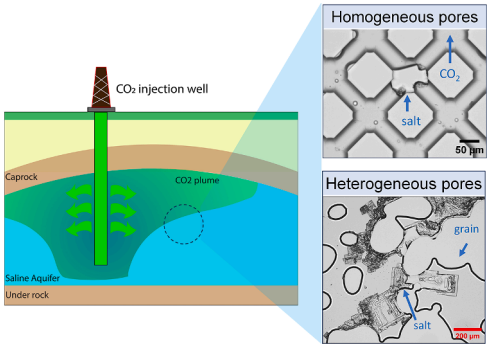

ARTICLE INFO

Keywords:
CO_2 subsurface storage
Salt precipitation
Saline water
Heterogeneity
Pore structure

ABSTRACT

CO_2 storage in deep saline aquifers is an effective strategy for reducing greenhouse gas emission. However, salt precipitation triggered by evaporation of water into injected dry CO_2 causes injectivity reduction. Predicting the distribution of precipitated salts and their impact on near-well permeability remains challenging. Therefore, a detailed investigation of the interactions between salt precipitation and porous domain is essential for of revealing the mechanisms of pore blockage due to salt crystallization. Through series of microfluidic experiments, direct observations, coupled with detailed imaging processing, form the basis for explaining these phenomena and provide a relationship between water and salt saturations, highlighting the critical roles played by local capillary-driven flow and water film along grains in influencing water relocation. The results reveal two distinct types of salt crystallization: occurring inside the brine with smooth edges and at the CO_2-brine interface with rough edges. Furthermore, the impact of local heterogeneity and surface wettability on salt precipitation patterns is discussed. The transition region between the porous domains and inlet/outlet channels exhibits brine backflow and a larger amount of salt accumulation. This paper presents a comprehensive analysis of the dynamic process of salt dry-out occurring during CO_2 injection at the pore scale.

* Corresponding author.
E-mail address: l.yan@tudelft.nl (L. Yan).

https://doi.org/10.1016/j.jcis.2024.08.265
Received 30 May 2024; Received in revised form 27 August 2024; Accepted 31 August 2024
Available online 2 September 2024

1. Introduction

In 2007, Intergovernmental Panel on Climate Change (IPCC) conclusively identified emissions of anthropogenic greenhouse gases as the primary and predominant driver of climate change and its subsequent environmental repercussions. Carbon dioxide (CO_2) assumes particular significance because of its disproportionately elevated concentration in the atmosphere compared to others (such as nitrous oxide and methane). The deployment of carbon capture and storage (CCS) in industrially challenging sectors for decarbonization, including ammonia, cement, long-distance sea, air transport and steel production, is poised to assume notable significance [1]. Approximately 95 % of the total CO_2 captured in 2050 is designated for permanent geological storage, with the remaining 5 % allocated for the synthesis of artificial fuels. The estimates for global geological storage capacity significantly exceed the necessary requirements to store the cumulative CO_2 captured and stored in the Net-Zero Emissions framework.

The sequestration of CO_2 in saline aquifers presents a practical avenue for accomplishing substantial global reductions in greenhouse gas emissions on the order of billions of metric tons annually [2]. The majority of saline formations globally are situated within sedimentary basins, which are likely to exhibit high porosity and permeability. The combination of large pores and high permeability in these geological formations results in a reduced need for numerous injection wells and facilitates smoother pressure dissipation [3]. Consequently, these saline formations boast substantial storage capacity compared to other geological structures. Storing CO_2 in deep subsurface reservoirs encounters a multitude of intricate challenges that inhibit a secure and effective storage process. The complex physical and chemical attributes of deep reservoirs, such as high salinity of brine, mineral precipitation and intricate geological structures, contribute to the inherent complexity of CO_2 storage within these formations [4]. Moreover, engineering factors including injectivity, pressure management, thermal exchange between borehole and reservoir, wellbore integrity, and the implementation of sustained monitoring procedures introduce substantial hurdles [5]. This work is dedicated to delving into pivotal challenges linked to the better understanding of salt precipitation affected by the porous structures at pore scale.

Within the process of CO_2 injection into subsurface reservoirs, the phenomenon of pore-scale salt precipitation holds significant importance due to its potential to impact the efficiency, safety, and environmental sustainability of these operations. Pore-scale salt precipitation can potentially jeopardize the long-term integrity of CO_2 storage sites, such as clogging of reservoir pores and reduced permeability, reduction of CO_2 injectivity, and brine backflow into the region near wellbore, influencing the overall success of CCS projects [6]. Due to lower density and viscosity of the displacing fluid (CO_2) compared to the resident brine, CO_2 displacement presents a spatial plume and a less-dense CO_2 front [7], as shown in Fig. 1(A).

The complex chemical and physical interactions between CO_2 and formation brine, e.g. pH decrease due to CO_2 dissolution and mineral precipitation, involve multiscale processes [8,9]. Water molecule diffuses into CO_2 flow and the salinity of brine gradually increases. Salt crystallization appears when brine salinity reaches the salting-out point. Salt precipitation occurs faster in the near-well area due to the high evaporation rate of water triggered by dry CO_2 flow, as shown in Fig. 1 (B). The interconnected salt crystal growing along the solid–gas–liquid interface occupies the pore space and throat, which reduces the permeability in the vicinity of the well. The reduction in injectivity due to salt precipitation can result in increased injection pressures. Smith et al. [10] reported significant injectivity reduction of a well located in the Quest CCS field in Canada due to the halite precipitation. After injecting a water-based fluid, the halite remediation was successfully achieved and the injectivity was recovered. As it becomes more difficult to inject CO_2 into the formation, higher pressures may be required to overcome the resistance caused by scale deposits. Elevated injection pressures can have safety implications and may also affect the structural integrity of injection wells and reservoir seals. In the unsaturated zone, brine undergoes disconnection into liquid clusters of varying sizes due to the continuous phase of CO_2. Prior to the CO_2 displacement front, there is a vaporization shock between dry-out zone and unsaturated zone [11].

One key question during CO_2 injection is how to reveal the mechanism of salt crystallization kinetics in pores and to quantify salt distribution and its influence on the reservoir properties. Several laboratory experiments and numerical simulations have proved that salt precipitation has the potential to change the porosity and permeability of the porous media [12]. Ott et al. [13] injected dry supercritical CO_2 into brine-saturated sandstone samples with 500 mD permeability and 0.22 porosity and measured effective permeability, fluid saturation, and salt saturation. They observed significant reductions in absolute permeability of CO_2 throughout the experiment. Peysson et al. [14] conducted flooding experiments utilizing X-ray attenuation techniques under 50 bar of confining pressure and temperatures of 90 °C and 120 °C to simulate dry CO_2 injection into deep saline aquifers. They observed a decrease in the CO_2 injection rate in Vosges sandstone after 26 h, reaching 0 l/min after 46 h, attributed to salt precipitation near the

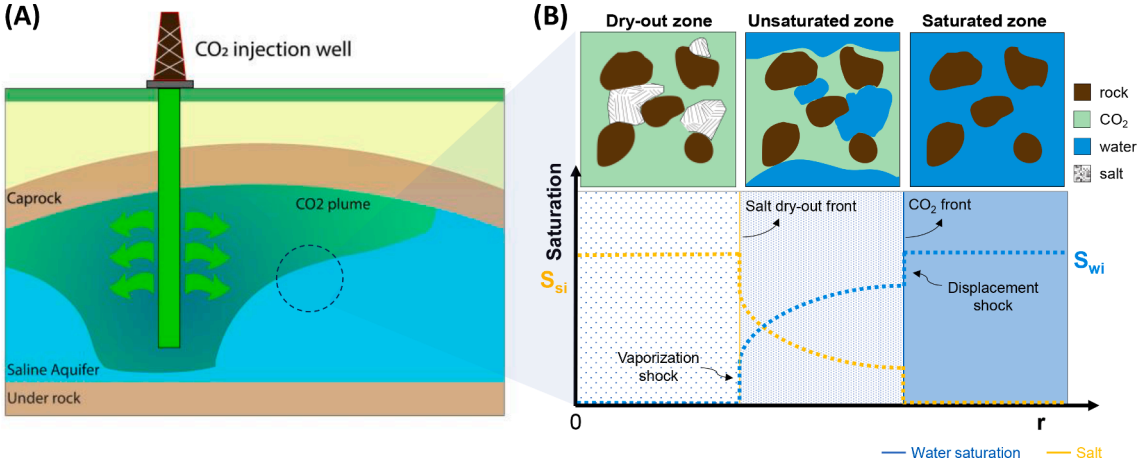

Fig. 1. Illustration of CO_2 injection in saline aquifers. (A), diagram depicting the injection of CO_2 into a saline aquifer. CO_2 plume forms during CO_2 injection due to CO_2 displacement in porous reservoir and buoyancy effect. (B), potential phase configurations near the wellbore, where S_{si} and S_{wi} are the initial saturations of salt and water, and r is the distance to the wellbore. Three zones are classified as, dry-out zone, CO_2 and brine saturated zone, and fully brine-saturated zone. Each zone has corresponding water and salt saturation.

wellbore and brine evaporation. Moreover, the permeability of the core was reduced by 70 %, with water saturation gradually diminishing until the core became completely dry. Their analysis indicated that drying represented the primary mechanism for water mass loss and pore clogging. Similar reductions in permeability during CO_2 injection were reported in other experimental studies, such as a 60 % reduction in Berea sandstone flooding [15], a 75 % reduction in St. Bees sandstone [16], and an 83 % reduction in Berea sandstone with 25 wt% brine [17]. Hence, it is imperative to incorporate the processes of water evaporation and salt precipitation into the pore space to ensure precise prediction of the distribution of salt and its impact on the physical properties of the reservoir.

Another issue during CO_2 injection is capillary-driven backflow near injection area of wellbore triggered by the capillary gradients of non-uniform water saturation and heterogeneity of the rock permeability. Direct observation of the capillary-driven backflow at the pore scale has been demonstrated in experimental work by Nachshon et al. [18]. The study provided insights into the mechanisms and impacts of capillary-driven backflow on porous media properties. This phenomenon supports observations at the core scale, indicating that capillary gradients induce backflow, influencing fluid dynamics and impacting porosity. Roels et al. [19] demonstrated that heterogeneous shapes of solid grains induce preferential locations for salt precipitation compared to uniform pore shapes. The study revealed that variations in pore shapes create localized zones with higher salt concentrations. The influence of the capillary-driven backflow on porosity and salt precipitation reveals that backflow alters local porosity, creating conditions favorable for increased salt precipitation in specific regions.

On the other hand, the unique geometry, connectivity, and tortuosity of pores within rock formations affect the initiation, growth, and distribution of salt crystals [20]. For instance, pore size significantly affects the drying kinetics [21]. From the perspective of the Gibbs-Thomson effect, the meniscus curvature leads to a reduction in the equilibrium vapor pressure of water in the confined pore [22]. Consequently, the patterns of the precipitated salt are largely influenced by pore size distribution. Therefore, it is essential for gaining insights into phenomena such as permeability alteration, pore plugging, and fluid channeling. While there is existing research on salt precipitation in porous media and studies on the impact of permeability and pore structure variations on fluid flow behavior, there is a lack of detailed analysis that directly connects these aspects. Few studies have delved into the intricate relationship between these factors and how they manifest at the pore scale [23,24]. Investigating this gap would involve conducting experiments or numerical simulations that systematically vary permeability distributions while monitoring salt precipitation behavior in real time. The findings from such research could provide valuable insights into optimizing CO_2 storage strategies, enhancing reservoir management techniques, and mitigating potential risks associated with salt precipitation-induced formation damage.

A quasi-2D micromodel is commonly employed to directly investigate multiphase flow behavior, mimicking the flow in a horizontal direction of real 3D rock [25,26]. The morphology and connectivity of the pore space determine the multiphase flow patterns formed, the shape of meniscus and the capillary trapping behavior of defending phase [27]. The uniformly wet surface of the 2D micromodel provides long-range connectivity of the wetting phase, resulting in precursor corner flow and/or thin-film flow along the porous structure [28,29]. The magnitude of wetting phase connectivity depends on surface roughness, geometry of designed pore pattern and wettability [30–32]. During water evaporation and salt precipitation, the brine saturation gradient induces capillary backflow that can be transported via the corner flow or/and thin-film flow [33]. Therefore, investigating the impact of pore structure and surface properties of the 2D micromodel on capillary-driven backflow during salt precipitation is essential [34].

This study aims to address three primary inquiries: firstly, the exploration of how variations in pore shapes within rock formations affect salt precipitation distribution, comparing uniform and heterogeneous structures; secondly, the localization of salt precipitation within the porous domain, specifically within pore throats or pore spaces; and finally, the influence of surface properties and boundary conditions, such as wettability and injection direction, on salt precipitation dynamics. Microfluidic experiments were conducted using two distinct grain structures. Section 2 delineates the experimental methodology and materials employed. Section 3 provides a comprehensive analysis of the results and subsequent discussion. Lastly, Sections 4 and 5 outline potential avenues for future research and summarize the conclusions drawn from this investigation.

2. Experimental materials and methods

2.1. Materials and microfluidic properties

Two distinct structures of micromodel are employed in this study, both sourced from Micronit Micro Technologies and constructed using borosilicate glass and fused silica materials. The micro-chips are fabricated through an acid chemical etching method, resulting in isotropic etching features. Each chip encompasses a porous media domain measuring 20 mm (length) × 10 mm (width). One type of microfluidic chip features a uniform (homogeneous) pore network characterized by a pore diameter of 90 μm and a throat width of 50 μm, as illustrated in Fig. 2 (A1). The other microfluidic chip is designed with rock-shaped (heterogeneous) structures to emulate the natural formations of rocks, as depicted in Fig. 2 (B1). In the porous domain of this chip, pore sizes range from 75 μm to 675 μm, with a median value of 275 μm, as shown in Fig. 2 (B3). The rationale behind using these two types of chips lies in the variation in the continuity of corner flow, which is influenced by different pore sizes. This variation gives significance for capillary-driven backflow. For the microfluidic chip with a uniform pore network, two variations are prepared with different surface wettability: water-wet (0–60° water contact angle) and intermediate-wet (60–100° water contact angle [35]). Additional properties of these microfluidic chips are detailed in Table 1.

2.2. Experimental set-up and procedure

A custom-designed experimental setup, depicted in Fig. 3, has been assembled for this study. The flow rate of CO_2, ranging from 0.007 to 0.7 ml/min, is precisely controlled using a mass flow controller sourced from Bronkhorst High-Tech B.V. (The Netherlands). To mitigate potential dust contamination in the inlet and outlet lines, Φ 0.25 μm filters are incorporated into the connecting lines. Brine, utilized in the experiments, is supplied by the QX Series Precision Pump. The imaging system comprises a Canon 750D camera body paired with an EF 100 mm f/2.8L Macro IS USM lens, offering an observation domain of 22.3 mm (length) × 14.9 mm (width) with a resolution of 3.7 μm/pixel. The maximum magnification of the lens is 5:1. The chip is securely positioned within a chip holder, resting on a light source, and interconnected with the system through tubes with an inner diameter of 0.25 mm.

We conduct six sets of experiments, as outlined in Table 2. Each experimental set is replicated twice to ensure result repeatability and consistency. During these experiments, the CO_2 injection direction is varied for both chips to systematically investigate the influence of heterogeneous pore structures on water and salt distribution. All experiments are carried out under atmospheric pressure and at a controlled temperature range of 30–33 °C. The brines used in the experiments are prepared by dissolving NaCl powder in deionized water to achieve one with 25 wt% concentration and one with 20 % wt% concentration. Notably, in the baseline experiments (No.5 and No.6), the deionized water is used without adding NaCl.

The experimental procedure is outlined as follows:

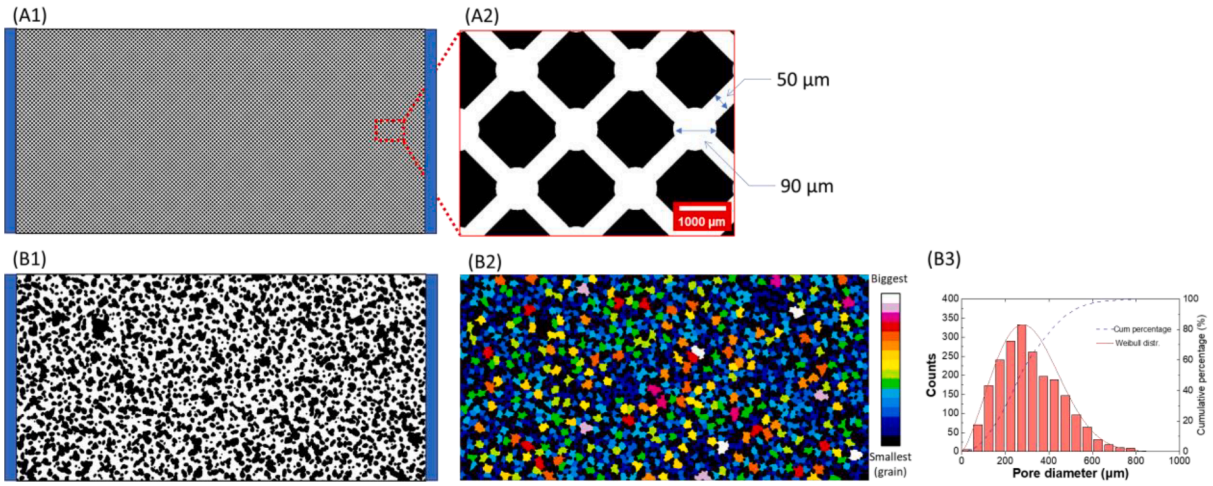

Fig. 2. Illustration of porous networks for two micro-models. Both micro-models feature inlet/outlet channels with a width of 0.5 mm on the left- and right-hand sides, indicated by the blue regions. In (A1), the micro-model displays a uniform porous network, where white represents pore space, and black represents solid grain. A magnified view of the uniform chip is presented in (A2). Moving to (B1), the micro-model displays a physical rock porous structure, while (B2) provides a segmented image of the physical rock chip. The smallest pore areas are depicted in black and white. (B3) offers insight into the pore size distribution of the pore space in the physical rock chip. The solid line represents a fitted Weibull distribution, and the dotted line indicates the cumulative percentage of pore size. (For interpretation of the references to color in this figure legend, the reader is referred to the web version of this article.)

Table 1
Properties of microfluidics.

Pore structure	Porosity	Permeability (Darcy)	Wettability (water contact angle)
Uniform (homogeneous)	0.52	9.29	intermediate water-wet (80) water-wet (40)
Physical rock (heterogeneous)	0.56	7.21	water-wet (40)

- Preparation for experiment: ensure chip cleanliness by removing surface dust. Optimize the camera and lens settings for capturing sharp focus on the pore region.
- CO_2 saturation: connect the inlet and outlet tubes to the chip. Initiate CO_2 injection at a flow rate of 0.035 ml/min for a duration of 10 min.
- Brine saturation: close the valve to the CO_2 mass flow controller and redirect the valve towards the effluent. Maintain brine injection at a flow rate of 0.01 ml/min until no gas bubbles are observed in the porous domain.
- CO_2 injection: open the CO_2 line and establish a connection to the outlet effluent. Inject CO_2 into the inlet line and chip at a controlled flow rate of 0.01 ml/min, set by the mass flow controller.
- Cleaning process: post-experiment, sequentially inject deionized water, ethanol, and another cycle of deionized water into the chip for one or two cycles until no contaminants are present. Place the cleaned chip in a vacuum oven and dry for 30–60 min at 70 ℃.

The image is processed using ImageJ with programmed macros. After binarizing and segmentizing the raw images, three phases (CO_2, salt and brine) are able to be visualized and quantified. Details and explanations of the image processing and data acquisition are provided in the Supplementary File.

Due to the difficulty in precisely controlling the local velocity of flow in the chip cross-section and the pores, we calculate the Log Ca-log M with an assumption that the CO_2 injection rate is 0.07 ml/min in our all

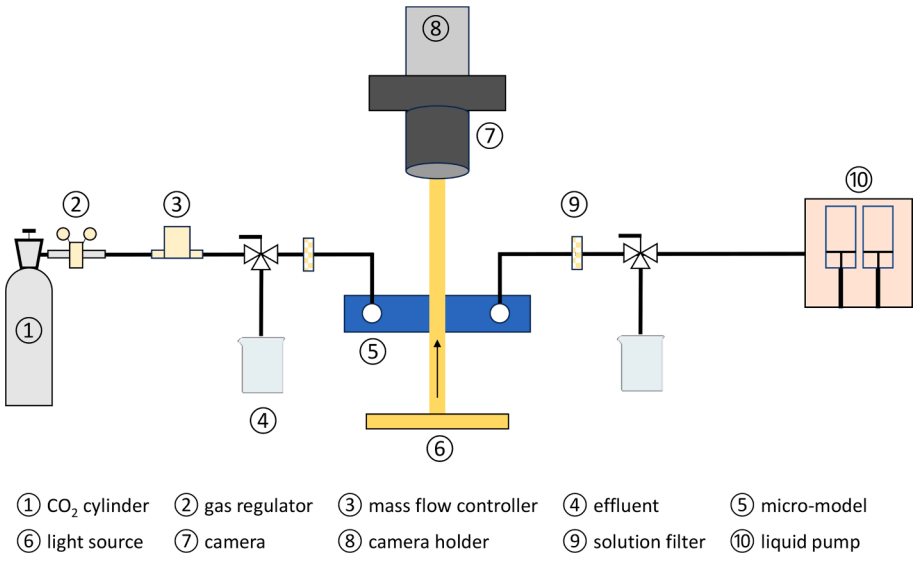

Fig. 3. Schematic of the experimental set-up.

Table 2
List of experiments for two types of microfluidic chips.

No.	Porous structure	Salinity (wt%)	Flow rate of CO_2 injection (ml/min)	Injection direction	Water contact angle
1	Uniform	20	0.01–0.07	→ and ←	80°
2		25			40°
3	Physical	20		→ and ←	
4	rock	25			
5	Uniform	0		→	
6	Rock				

experiments. The details of calculation method for two-phase flow in the micromodel is described in the supplementary file. The CO_2-brine displacement performs as capillary fingering for the case of considering the whole micromodel as a rectangular channel (w = 10,000 μm for capillary number calculation), while it performs in the transition regime for the case of considering the lowest diameter in the uniform chip (w = 50 μm for capillary number calculation), as shown in Fig. 4. The fractal dimensions are 1.72 and 1.61 for the homogeneous and heterogeneous porous media, which indicating that both CO_2 displacements of water preform relatively complex and irregular displacement patterns but the displacement process in the heterogeneous chip is smoother.

Following CO_2 displacement, the CO_2/water interface presents distinct meniscus shapes and contacting areas in the two chips, as shown in Fig. 4 (C). Heterogeneous grain patterns allow water staying as relatively larger clusters at local areas compared to the homogeneous chip. Moreover, the heterogeneous chip exhibits fewer flow paths and smaller-size fingers for CO_2 flow, attributed to the connectivity of the pore network. Wettability plays a crucial role in determining the connectivity of the wetting phase [27]. With a water-wet surface ($\theta_w \approx 40^\circ$), the pore-scale CO_2/water menisci exhibits strong water wetness. Consequently, the chance to gain a long-range continuity of water through corner/thin-film flow is higher than that observed with an intermediate-wet surface [36].

3. Result and discussion

3.1. Dynamics of salt crystallization and propagation at pore scale

Based on the processed images, we can capture the dynamic processes of salt crystallization and growth within the pore after salt nucleation at the solid surface, as depicted in Fig. 5. In Fig. 5 (B), sizable salt crystallization occurs in the brine when the salinity reaches the super saturation point. It grows in two directions: one within the brine with smooth edges distant from the CO_2-brine interface and the other along the interface. The propagation at the CO_2-brine interface exhibits polycrystalline aggregated structures of salt accumulation. At the shrinking solid–liquid-gas interface, capillary forces enhance curvature and reduce radii of curvature, where the water becomes more confined. These regions often serve as preferred sites for nucleation because the confined space can locally supersaturate the dissolved salts, lowering the energy barrier for nucleation. This observation is consistent with the findings of Kim, et al. (2013) [37]. This shape is clearly depicted under 3D reconstruction of the microscope (Fig. 5D). An interesting observation is that when the CO_2-brine interface approaches the salt edge in the brine at 210 min, the interface is stretched to a curved meniscus due to the naturally hydrophilic property of salt crystals [38]. After about 320 min, the salt crystal establishes its basic shape in the brine and most of the water evaporates. The remaining brine begins to accumulate in the gap between the surfaces of the salt and the glass micromodel, which forms the rough top surface after all brine evaporation at 350 min. The evaporation rate of water is calculated 411.3 μm^2/min, while the precipitation rate of salt is estimated to be 94.5 μm^2/min, as shown in Fig. 5C.

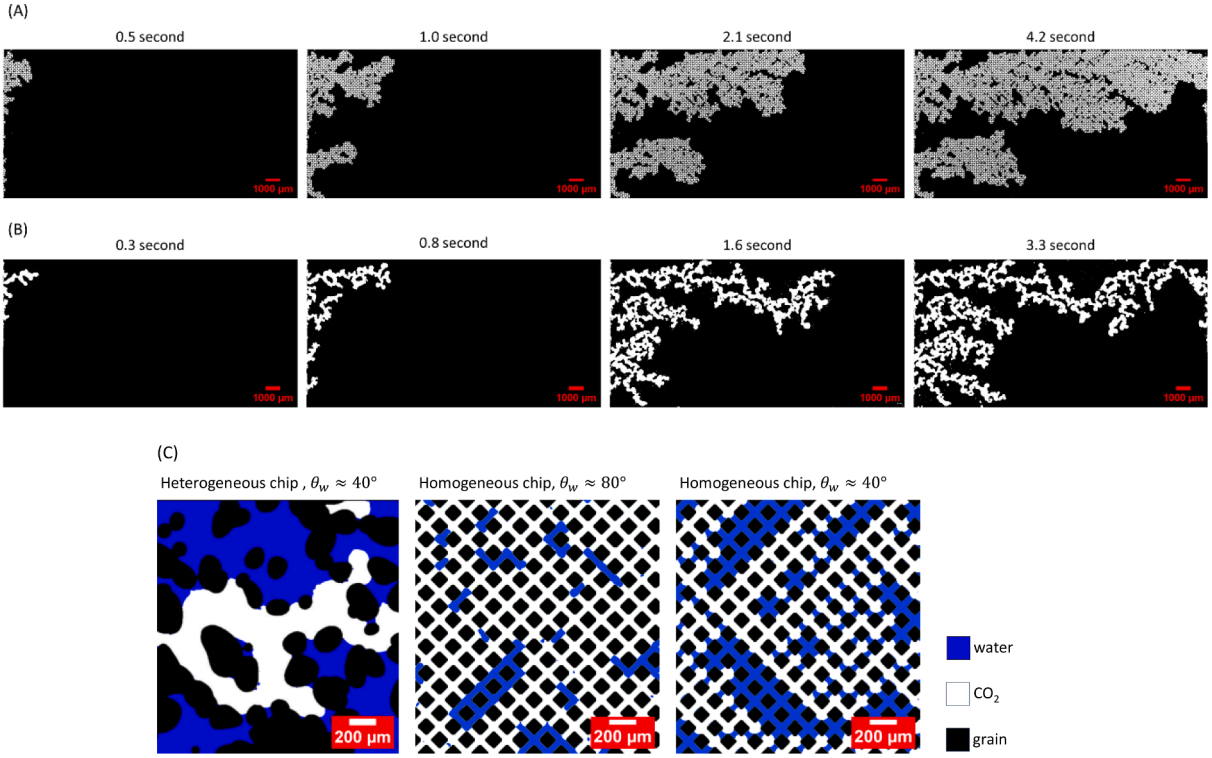

Fig. 4. Images of CO_2 displacement for the homogeneous micromodel (A), heterogeneous micromodel (B) and CO_2/water interfaces after CO_2 displacement in two micromodels under two wettability (C). In (A) and (B), white phase represents the CO_2 phase and black represents water and grain areas. The time above pictures indicate the displacement moments to the invading CO_2 phase into the porous media.

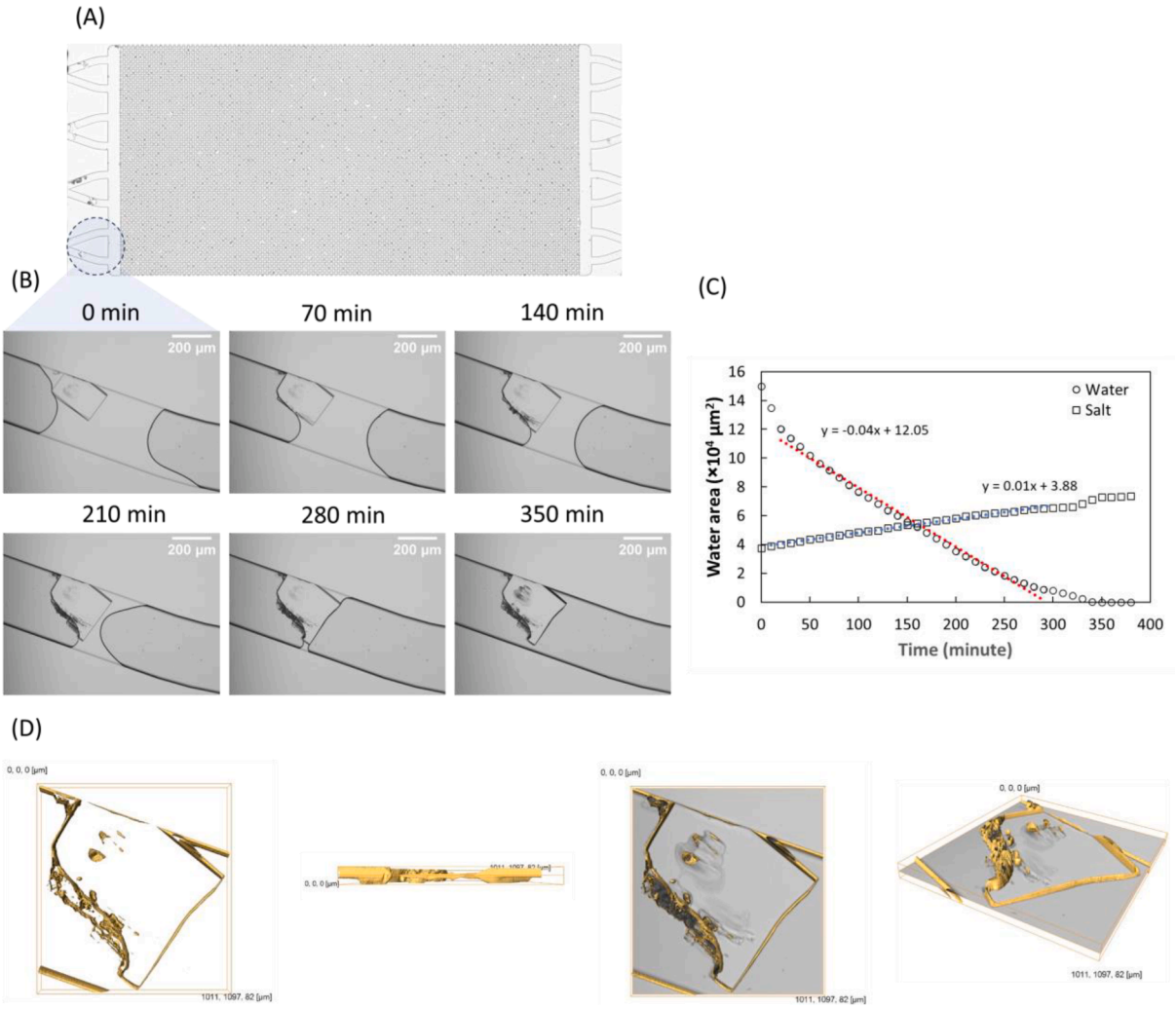

Fig. 5. Pictures of salt crystallization and growth in a microfluidic channel. (A) Gives the whole image of the uniform microfluidic. The salt crystals precipitates in the porous media domain as black dots. One specific crystal is observed under a zoomed view, as shown in (B). The crystal growth is captured with 380 mins. And the water and salt areas are measured and plotted in (C). (D) Provides the 3D reconstruction and the edges in a golden color.

3.2. Dynamic of salt precipitation in two pore structures

Pore structure, including pore–throat ratio, shape heterogeneity, pore connectivity, and curvature leads to various water distributions after CO_2 displacement due to the local capillary pressure [39]. Although the injection rate determines the water distribution, the water cluster and CO_2 distribution are highly dependent on the pore and throat structures. In our homogeneous micromodel, the uniform pore network with a pore diameter of 90 μm and throat width of 50 μm results in irregular water distribution due to the fingering displacement of CO_2. With the continuous water evaporation into dry CO_2 flow and the onset of salt crystallization, the dry-out front appears as a relatively vertical line and displays piston movement towards the end boundary of the porous domain, as depicted in Fig. 6 (A). Large water clusters form large salt crystals; therefore, most salt precipitates in the pore and throat, exhibiting a star-like distribution. The heterogeneous pore structure exhibits a diverse array of brine clusters after CO_2 displacement, as shown in Fig. 6 (B). Approximately 30 h into the experiment, the entire chip undergoes drying. In contrast to experiments with homogeneous chips, salt begins to crystallize along the CO_2-brine-grain interface and propagates in spatial directions within pore spaces until reaching another solid surface. Additionally, residual brine exhibits sporadic and uneven distribution. However, despite the presence of large brine clusters, significant salt accumulations do not form. The varied pore spaces and throats permit higher irregularity in salt propagation within the porous domain compared to homogeneous pore structures, contingent upon pore connectivity. Salt crystals form at interfaces and absorb water from connecting brine. The location of brine can be altered by capillary flow along the grain surface water film, consistent with the mechanism of self-enhancing salt nucleation and precipitation [33].

Dynamic water and salt saturations for two pore structures are plotted in Fig. 6 (C). In the homogeneous pore structure, approximately 28 % of the pore space is initially occupied by water. As the experiment progresses, the saturations of salt and water perform three stages. In the first stage, the water saturation gradually decreases at a rate of 1.70×10^5 μm^2/hour, indicating the gradual evaporation of water into CO_2 flow from the residual brine. CO_2 flow can bring the water molecular throughout the whole chip from inlet region to the end, which induces the slow decrease in system humidity. With the appearance of the dry-out front, water rapidly diffuses into dry CO_2 flow and salt is introduced into the system, resulting in a linear increase in salt saturation over time. The rate of increase in salt saturation varies throughout the experiment, showing periods of rapid increase followed by slower increments. This pattern reflects the dynamic changes in water and salt infiltration and distribution within the porous medium over time. The rate of water disappearance in the second stage is 1.03×10^6 μm^2/hour, while the rate of salt accumulation is 1.09×10^5 μm^2/hour. Eventually, as the experiment enters the third stage, the salt saturation stabilizes at

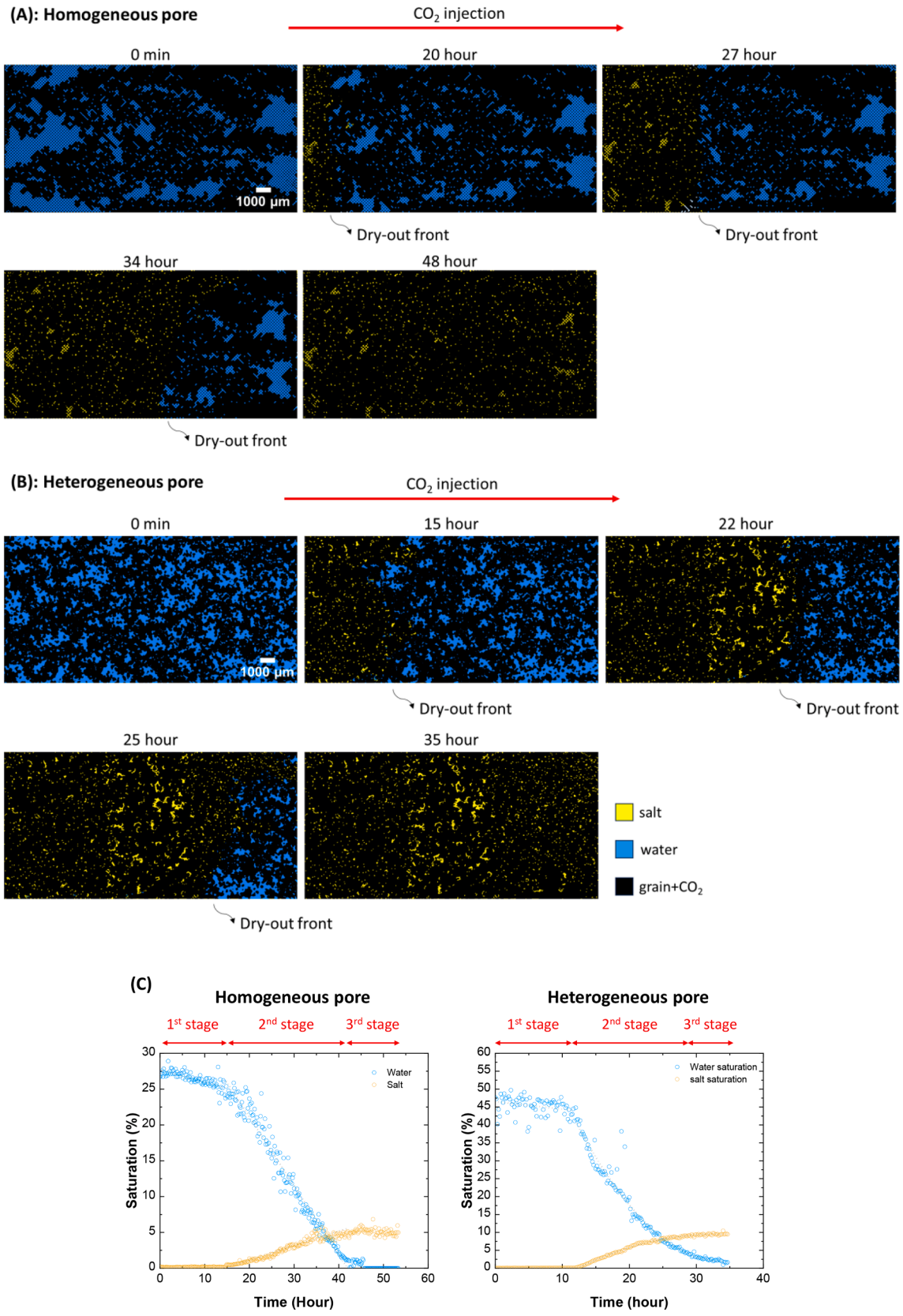

Fig. 6. Experimental pictures and analysis of dynamic salt precipitation in two pore structures (the cases with 20 wt% NaCl brine), homogeneous pore (A), heterogeneous pore (B) and dynamic saturations of water and salt (C).

around 5.3 % due to the overall loss of water in the domain. This figure intuitively demonstrates how the saturation of water and salt changes over time during the experiment and can be used to deduct the parameters of salt precipitation kinetics for homogeneous porous media. In the heterogeneous pore structure, the initial water saturation is approximately 45 %, significantly higher than the observed water saturation in homogeneous chips (both water-wet and intermediate-wet chips). Due to varying local capillary pressures, the heterogeneous pore structure has the potential to retain more water. Additionally, the chip exhibits three stages of water and salt saturation, similar to what is observed in homogeneous chips. An interesting phenomenon is noted where the changes in water and salt saturation during the second stage do not follow a linear trend. The final salt saturation reaches approximately 9.5 %, about 1.9 times higher than that in uniform chips.

The typical processes of salt crystallization and growth for both structures are captured and depicted in the Appendix section. Furthermore, to evaluate the favorable position of salt precipitation, we split the whole chip domain into three sections first and then measure the area of salt in each section. The measurement reveals that the salt position and size are consistent with the initial pore distribution and space. In the heterogenous pores, the irregular growth of salt crystals leads to distinct types of pore space blockage. Accumulated salt exhibits rougher shapes compared to those in homogeneous chips.

3.3. Impact of local heterogeneity on salt precipitation

To investigate the influence of local heterogeneity (pore connectivity) on salt precipitation and distribution, we conduct additional experiments using reverse CO_2 injection directions. The experimental results in heterogeneous chips are presented in Fig. 7. We notice that changing the injection direction does not affect the overall trend of salt distribution in homogeneous porous media. Therefore, we refrain from reiterating here and focus solely on the detailed analysis of heterogeneous media. In the two figures, we demonstrate the dynamic distributions of brine along the X-axis of the chip, the final salt distribution, and the initial pore distribution for both injecting directions. The left figure displays the outcome of CO_2 injection from left to right, whereas the right figure depicts the reverse injection scenario.

The water-wet microfluidics tend to exhibit higher water saturations near the outlet due to the capillary-end effect [40]. The capillary-end effect and local water movement are also captured in the heterogeneous microfluidics. There is also an initial water saturation near the outlet. However, with the occurrence of salt precipitation and continued water evaporation, there is lower salt distribution near the outlet. Conversely, more salt accumulates near the inlet due to the capillary-driven cross flow among grains. Local porosity and permeability decreases as a result of salt nucleation and aggregation, leading to differences in capillary forces that causes the water movement from the region with higher water saturation to the region with lower water saturation [41]. Initial salt particles form thin water layers due to the hydrophilicity of salt itself. The water-wet pore structure provides well-connected water films, allowing salt particles to strongly absorb saltwater over long distances towards the evaporation front. Subsequently, the absorbed saltwater continues to evaporate on the aggregate, resulting in more precipitation. This phenomenon is similar to the one observed in Fig. 5. This mechanism is reported in other experimental and numerical studies [33,42], and we provide more direct evidence for it.

Additionally, it is observed that the location of salt precipitation is different due to local heterogeneity. When CO_2 gas displaces from left to right, the central pores of the heterogeneous microfluidic chip have more salt deposition. When the injection direction changes, more salt accumulates near the right region. This is not an isolated occurrence in a single experiment; rather, this significant difference appeared consistently in our repeated experiments with various heterogeneous microfluidic chips. Furthermore, in the supplementary materials, we found that in heterogeneous porous media, the direction of salt crystal growth is opposite to the direction of CO_2 injection. This phenomenon is not observed prominently in homogeneous microfluidic chips.

3.4. Impact of brine salinity on salt precipitation

20 wt% and 25 wt% NaCl solutions were used as saline water or brine, as shown in the supplementary materials. We investigate the effect of different salt concentrations on local salt morphology in two microfluidic chips. Overall, the 25 wt% saline water resulted in larger and more easily formed salt crystal particles, as depicted in the bar chart in the figure. Salt particles formed by the 20 wt% saline water exhibited more individual grains. In the uniform pores, salt crystal grains are dispersed, blocking individual circular pores, with some salt aggregating into transparent larger particles that block multiple rectangular channels and adjacent pores. In heterogeneous pores, although multiple independent salt particles are formed by the 20 wt% saline water, many of them are located in concave dead-end pores. In contrast, with the 25 wt % saline water, besides observing larger salt particles with rougher appearances, multiple small salt particles were also found to appear in a branched, feather-like form. This is due to the trace residual water on the surface of the salt nuclei moving slowly along the crystal branches towards the dry-out direction during water evaporation, gradually accumulating longer crystal branches

3.5. Impact of wettability on the salt precipitation

We observe that the salt precipitates more along the top and bottom edges of the water-wet chip close to the inlet regions due to longer and thicker brine films along these edges, as shown in the Appendix. CO_2 phase exists in the water-wet chip as long strings and individual circles

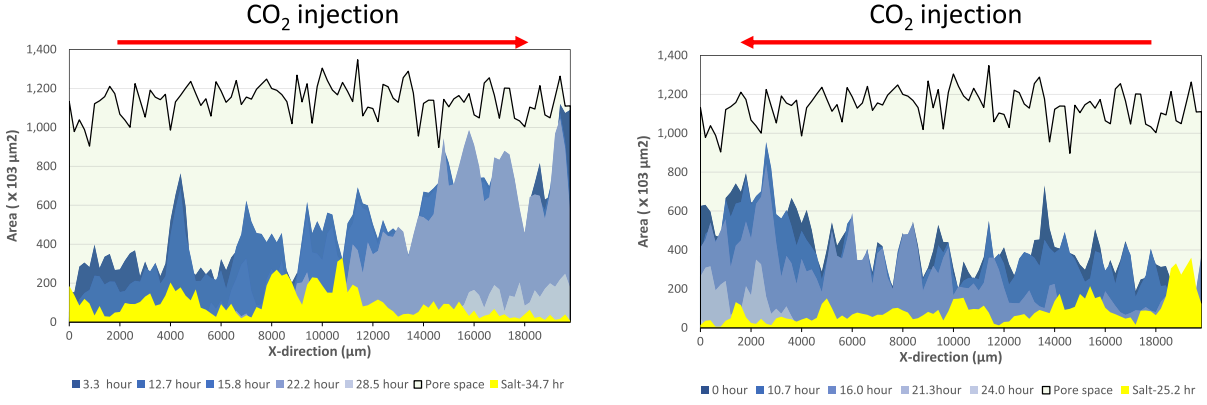

Fig. 7. Brine distribution (blue areas), salt distribution (yellow area) and initial pore distribution (black line and green shadow) in the x-direction of two heterogeneous chips. (For interpretation of the references to color in this figure legend, the reader is referred to the web version of this article.)

trapped in the pores. Additionally, the salt clusters exhibit different patterns in both chips. The water-wet chip contains larger salt crystals (mean feret diameter except, 59.7 μm) owing to the presence of stronger wettability. Stronger water-wet surface maintains more water thin-film and corner flow [36] and consequently aggregates a higher mass of salt. Conversely, the intermediate-wet chip is characterized by pore-sized salt particles (median size, 40.8 μm) formed from the less amount of water absorbed by the surface. Note that the salt particle size refers to an average value and does not exclude the possibility that large salt clusters form locally due to the accumulations of brine in the intermediate-wet chip. Although the water-wet chip leads to higher residual water in the outlet region, the final salt distribution along the X-direction of the chip remains relatively uniform. This suggests that the brine has redistributed through a thin water film along the glass surface during CO_2 displacement and water evaporation [34]. Furthermore, the water-wet chip exhibits a higher salt saturation (7.70 %) in the final stage compared to that in the intermediate-wet chip (5.12 %).

3.6. Comparison results of water loss and salt precipitation for all experiments

We computed the average initial residual water saturation and final salt saturation for all experiments to differentiate the effects of wettability, injection direction, and pore structure, as shown in Fig. 8 (A). The results indicate that hydrophilic homogeneous pores retain 6.51 % more residual water compared to weakly hydrophilic pores, resulting in a 2.38 % increase in salt deposition. Moreover, heterogeneous pores can retain more residual water. In the control experiment (with pure water and no salt), heterogeneous pores retain nearly 9.44 % more residual water compared to the homogeneous pores. In the experiments involving saline water, heterogeneous pores contain 10.27 % more residual water than homogeneous pores and exhibit a 1.32 % higher final salt saturation. Injection direction has minimal influence on the initial water saturation after CO_2 displacement in both homogeneous and heterogeneous porous media. However, it significantly affects the distribution morphology and location of salt particles in the heterogeneous pores.

Furthermore, we calculated the rates of dynamic water and salt changes in all 13 experiments to gain a clearer understanding of the dynamic salt precipitation kinetics, as shown in the Fig. 8 (B). The results indicate that prior to the appearance of the dry-out front, there is a slight evaporation of residual water. In the neutrally wet homogeneous chip, the rate of brine evaporation is 1.8×10^5 μm^2/hour. In the water-wet homogeneous chip, this value increases by a factor of 3.2. Even in the comparison chip experiments, there is 1.8 times increase in this value. When the dry-out front appears, the rate of water mass loss accelerates by an order of magnitude. Meanwhile, the results of salt precipitation rates also indicate that water-wet surfaces exhibit faster salt deposition. Both water-wet homogeneous and heterogeneous chips have similar salt precipitation speeds, approximately 1.0×10^6 μm^2/hour, which is four times that of the neutrally wet chip.

3.7. Observation of capillary-driven backflow at pore-scale

In the experiments, we observed a phenomenon of water backflow either inside the chip or in the inlet regions, as shown in the supplementary file. The backflow occurred near the outlet after the appearance of the dry-out front, where a small amount of water flowed back into the chip through outlet channels. This invading water results in a slight increase in the residual brine saturation within the chip (shaded in light blue in the Fig. 9 (A)). The water backflow may be attributed to the local capillary pressure gradient dragging the brine droplets retained on the surface of the chip outlet. This phenomenon has also been captured in core displacement experiments, especially in heterogeneous cores [19]. Throughout this process, the salt saturation remained unchanged. When the dry-out front reached the backflow area, the salt saturation experienced a second increase (shaded in yellow in the Fig. 9 (A)), with the salt precipitation rate essentially consistent with the first instance, until reaching a second steady state.

Another water backflow and salt accumulation are observed at the injection inlet regions in two microfluidic chips, where the permeability and local flow velocity suddenly change, as shown in Fig. 9 (B). Following the completion of CO_2 injection displacement, a small additional amount of saltwater (approximately 0.1 μL) infiltrated near the inlet, causing a localized increase in water saturation in the infiltrating water zone. Salt nucleation and accumulation occurred in the transition zone between the inlet channel and the porous medium. The narrowing of local pores resulted in differential capillary forces, sustaining the supply of saltwater to these deposited salts, eventually leading to significant deposition at the inlet channel. Additionally, corner flow gives a potential mechanism for the formation of localized salt, particularly in regions with long-range brine connectivity. Conversely, in scenarios where salt is uniformly dispersed across the micromodel, the occurrence of corner flow is less likely [34,43]. If the initially large interconnected water gradually separates into multiple individual regions during evaporation, a phenomenon similar to the salt deposition observed in other experimental chips, where large salt particles form within the porous medium rather than in the injection channels, occurs. This capillary-driven backflow bears a striking resemblance to the easier accumulation of salt at the gap between the injection port and the core in core displacement [13]. However, the primary difference lies in the difficulty of achieving good water connectivity and sustained supply in 2D microfluidic chips compared to 3D cores.

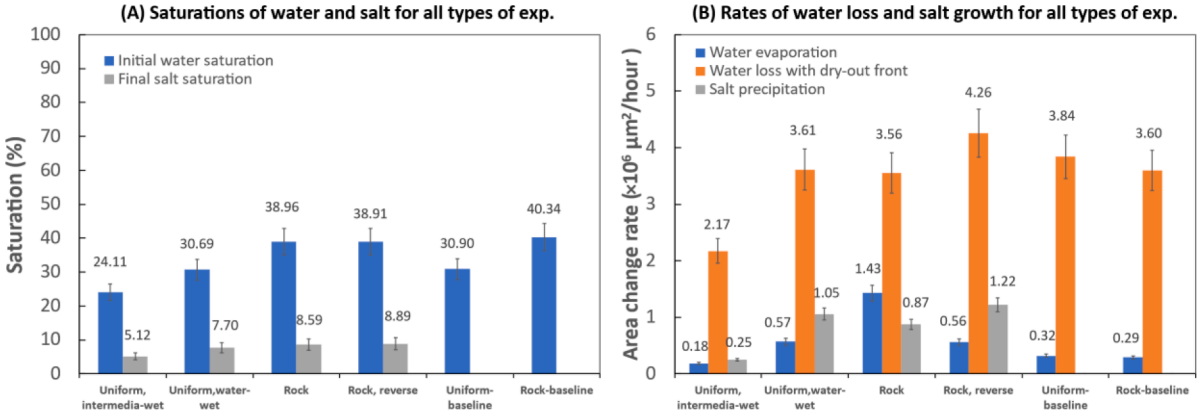

Fig. 8. Initial water saturation and final salt saturation in various experiments for both chips (A) and averaged rates of water loss and salt growth in two chips. The measurement error is 10%.

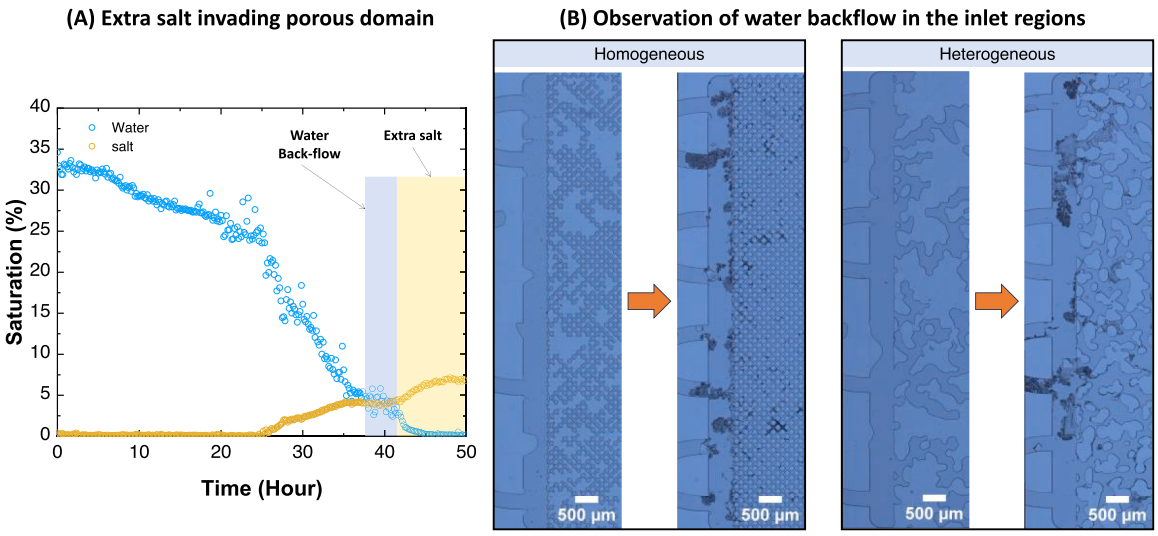

Fig. 9. Capillary-driven backflow in the intermediate-wet homogeneous chip (A) and observation of water backflow in the inlet regions (B).

4. Future research

More investigations on gas–liquid interface and corner flow are necessary. Although our study has distinguished the contact area between CO_2 and brine, the direct observation of corner flow and its connectivity is still lacking. Additionally, the connectivity of the corner flow network is crucial for facilitating water backflow, which results in diverse salt patterns or local salt saturation [27]. The heterogeneity of the pore structure yields significantly different corner flow patterns depending on local pore and throat sizes, as well as wettability [44]. Thus, the relationship between salt precipitation and corner flow is one of our future researches.

Diffusion rate of water into CO_2 flow at the various reservoir conditions still needs to be determined. When liquid CO_2 is injected in the depleted field, it induces the Joule-Thomson effect, which refers to the isenthalpic temperature change accompanying gas expansion [45]. The impact of this phenomenon on the rates of water evaporation and salt precipitation requires further investigation. It can be anticipated that during Joule-Thomson cooling, there is a sharp decrease in temperature around the injection well, leading to reduced rates of water evaporation and salt precipitation. In regions farther away from the injection well, temperatures approach the formation temperature, resulting in a significant increase in salt precipitation rates [46]. Determining the primary areas of salt precipitation is crucial as it directly affects the efficiency of CO_2 injection and amount of trapped CO_2 due to solubility [47].

Another aspect includes how to integrate results from 2D and 3D experiments and apply them to large-scale numerical simulations. While many researchers have conducted 3D imaging scans of salt precipitation [9,48,49], limitations in time and image resolution restrict the observed directions and ranges. 2D chip experiments can provide highly accurate results but suffer from reduced pore connectivity compared to 3D cores. This limitation may explain why large-scale salt precipitation near the injection point, accompanied by a significant decrease in injection rates, observed in 3D experiments is challenging to reproduce in 2D chip experiments. Therefore, effectively combining results from these two scales or finding a more optimized imaging approach could provide more accurate data for large-scale numerical simulations.

5. Conclusions

This work provides a detailed explanation of the dynamic nucleation of salt precipitation at the solid–liquid–gas interface, as well as the impact of local capillary forces on the migration of residual water and salt precipitation. We conducted micro-scale glass chip experiments to investigate kinetics of salt precipitation and the effects on porous media properties. Two types of pore structures, homogeneous and heterogeneous, were employed, along with two different wettability levels of homogeneous chips, in replicable experiments. Through image processing, we achieved dynamic monitoring and quantitative analysis of residual brine and salt precipitation processes. The following conclusions can be drawn:

In porous media, water evaporation and salt deposition can be divided into three stages: slow water evaporation (during this stage, water molecules diffuse into CO_2 channels, but the entire porous media still retains some humidity), rapid water evaporation (after the dry-out front appears, a large number of water molecules rapidly diffuse into the dry CO_2 flow, and salt precipitation occurs simultaneously.), and water evaporation completion (at this point, the water saturation in the entire porous media is zero, and the salt saturation remains stable). Although some studies have shown the similar description [50,51], our work provides a detailed description of the changes in water and salt in the heterogeneous pores before and after the dry-out front during CO_2 injection.

Under our experimental conditions, pore structure has a significant influence on the initial water saturation and the final distribution morphology of salt. Heterogeneous pores can capture more initial brine due to irregular pore shapes and larger pore diameters, resulting in higher salt saturation and more continuous and larger salt crystals. Homogeneous porous media form a relatively homogeneous distribution with salt crystals similar in size of pores. The role of local heterogeneity in causing water backflow and its effect on salt precipitation is still questionable [52]. In our experiments, capillary crossflow and capillary backflow are directly observed. The effect of local capillarity is revealed in salt precipitation experiments in the heterogeneous chip when injection direction is reversed, resulting in different patterns of salt distribution. Additionally, due to the capillary-driven backflow, more salt aggregates in regions close to the CO_2 injection points.

Surface wettability affects the kinetics of water evaporation and salt precipitation. Intermediate-wet porous media exhibits slower rates of water evaporation and salt precipitation. Although several studies illustrate the wettability effect [34,53], its quantitate influence on the kinetics of salt still needs to be deeply understood. In contrast, water-wet surfaces produce larger diameter salt crystals (approximately 1.6 times larger than those in neutral-wet media) and higher final salt saturation. Our experiments showed that the chips with water-wet surfaces exhibit water movement during salt precipitation, primarily due to the possible long-range connectivity of water corner flow, resulting in salt

accumulation within the large water. The salt precipitation induces local permeability reduction where capillary crossflow occurs and moves through water corner or/and films on grain surfaces, resulting in differences in final salt saturation.

Future research directions could focus on three primary areas based on the existing experimental foundation: investigation of corner flow and its effect on the salt precipitation, water evaporation and salt precipitation under the reservoir conditions, and upscaling experimental results from pore scale to reservoir scale.

CRediT authorship contribution statement

Lifei Yan: Writing – review & editing, Writing – original draft, Visualization, Investigation, Conceptualization. **Rustam Niftaliyev:** Data curation. **Denis Voskov:** Writing – review & editing, Supervision. **Rouhi Farajzadeh:** Writing – review & editing, Supervision.

Declaration of competing interest

The authors declare that they have no known competing financial interests or personal relationships that could have appeared to influence the work reported in this paper.

Data availability

Data will be made available on request.

Acknowledgement

Authors thank Shell Global Solutions International for granting permission to publish this work. Steffen Berg is acknowledged for detailed review of the draft manuscript.

Appendix A. Supplementary material

Supplementary data to this article can be found online at https://doi.org/10.1016/j.jcis.2024.08.265.

References

[1] A. Hansson, J. Anshelm, M. Fridahl, et al., The underworld of tomorrow? How subsurface carbon dioxide storage leaked out of the public debate, Energy Res. Soc. Sci. 90 (2022) 102606, https://doi.org/10.1016/j.erss.2022.102606.
[2] S. Kumar, J. Foroozesh, K. Edlmann, et al., A comprehensive review of value-added CO_2 sequestration in subsurface saline aquifers, J. Nat. Gas Sci. Eng. 81 (2020) 103437, https://doi.org/10.1016/j.jngse.2020.103437.
[3] M. Bentham, G. Kirby, CO_2 storage in saline aquifers, Oil Gas Sci. Technol.-Rev. D Ifp Energ. Nouvelles. 60 (3) (2005) 559–567, https://doi.org/10.2516/ogst:2005038.
[4] R.T. Mim, B.M. Negash, S.R. Jufar, et al., Minireview on CO_2 storage in deep saline aquifers: methods, opportunities, challenges, and perspectives, Energy Fuel 37 (23) (2023) 18467–18484, https://doi.org/10.1021/acs.energyfuels.3c03185.
[5] M.V.B. Machado, M. Delshad, K. Sepehrnoori, Injectivity assessment for ccs field-scale projects with considerations of salt deposition, mineral dissolution, fines migration, hydrate formation, and non-darcy flow, Fuel 353 (2023) 129148, https://doi.org/10.1016/j.fuel.2023.129148.
[6] E. Guyant, W.S. Han, K.Y. Kim, et al., Salt precipitation and CO_2/brine flow distribution under different injection well completions, Int. J. Greenhouse Gas Control 37 (2015) 299–310, https://doi.org/10.1016/j.ijggc.2015.03.020.
[7] J.M. Nordbotten, M.A. Celia, S. Bachu, Injection and storage of CO_2 in deep saline aquifers: analytical solution for CO_2 plume evolution during injection, Transp. Porous Media 58 (3) (2005) 339–360, https://doi.org/10.1007/s11242-004-0670-9.
[8] D.V. Voskov, H. Henley, A. Lucia, Fully compositional multi-scale reservoir simulation of various CO_2 sequestration mechanisms, Comput. Chem. Eng. 96 (2017) 183–195, https://doi.org/10.1016/j.compchemeng.2016.09.021.
[9] D. Akindipe, S. Saraji, M. Piri, Salt precipitation during geological sequestration of supercritical CO_2 in saline aquifers: a pore-scale experimental investigation, Adv. Water Resour. 155 (2021) 104011, https://doi.org/10.1016/j.advwatres.2021.104011.
[10] N. Smith, P. Boone, A. Oguntimehin, et al., Quest ccs facility: halite damage and injectivity remediation in CO_2 injection wells, Int. J. Greenhouse Gas Control 119 (2022) 103718, https://doi.org/10.1016/j.ijggc.2022.103718.
[11] S. de Hoop, D. Voskov, E. Ahusborde, et al., A benchmark study on reactive two-phase flow in porous media: Part i-model description, Comput. Geosci. 28 (1) (2024) 1–15, https://doi.org/10.1007/s10596-024-10268-z.
[12] R. Miri, H. Hellevang, Salt precipitation during CO_2 storage-a review, Int. J. Greenhouse Gas Control 51 (2016) 136–147, https://doi.org/10.1016/j.ijggc.2016.05.015.
[13] H. Ott, S.M. Roels, K. de Kloe, Salt precipitation due to supercritical gas injection: I. Capillary-driven flow in unimodal sandstone, Int. J. Greenhouse Gas Control 43 (2015) 247–255, https://doi.org/10.1016/j.ijggc.2015.01.005.
[14] Y. Peysson, L. André, M. Azaroual, Well injectivity during CO_2 storage operations in deep saline aquifers-part 1: Experimental investigation of drying effects, salt precipitation and capillary forces, Int. J. Greenhouse Gas Control 22 (2014) 291–300, https://doi.org/10.1016/j.ijggc.2013.10.031.
[15] N. Muller, R. Qi, E. Mackie, et al., CO_2 injection impairment due to halite precipitation, Greenhouse Gas Control Technol. 9 1 (1) (2009) 3507–3514, https://doi.org/10.1016/j.egypro.2009.02.143.
[16] G. Bacci, A. Korre, S. Durucan, Experimental investigation into salt precipitation during CO_2 injection in saline aquifers, in: 10th International Conference on Greenhouse Gas Control Technologies, vol. 4, 2011, pp. 4450–4456. doi:10.1016/j.egypro.2011.02.399.
[17] Y. Tang, R.Z. Yang, Z.M. Du, et al., Experimental study of formation damage caused by complete water vaporization and salt precipitation in sandstone reservoirs, Transp. Porous Media 107 (1) (2015) 205–218, https://doi.org/10.1007/s11242-014-0433-1.
[18] U. Nachshon, N. Weisbrod, M.I. Dragila, et al., Combined evaporation and salt precipitation in homogeneous and heterogeneous porous media, Water Resour. Res. 47 (3) (2011), https://doi.org/10.1029/2010wr009677.
[19] S.M. Roels, N. El Chatib, C. Nicolaides, et al., Capillary-driven transport of dissolved salt to the drying zone during CO_2 injection in homogeneous and layered porous media, Transp. Porous Media 111 (2) (2016) 411–424, https://doi.org/10.1007/s11242-015-0601-y.
[20] M.N. Rad, N. Shokri, A. Keshmiri, et al., Effects of grain and pore size on salt precipitation during evaporation from porous media, Transp. Porous Media 110 (2) (2015) 281–294, https://doi.org/10.1007/s11242-015-0515-8.
[21] H.T. Vu, Influence of Pore Size Distribution on Drying Behaviour of Porous Media by a Continuous Model, Otto-von-Guericke-Universität Magdeburg, Universitätsbibliothek, 2006.
[22] Sparavigna A.C. Water in Pores: The Gibbs-Thomson Effect, 2023. Available at SSRN 4349640. doi:10.2139/ssrn.4349640.
[23] H. Dashtian, N. Shokri, M. Sahimi, Pore-network model of evaporation-induced salt precipitation in porous media: the effect of correlations and heterogeneity, Adv. Water Resour. 112 (2018) 59–71, https://doi.org/10.1016/j.advwatres.2017.12.004.
[24] A.H. Alizadeh, M. Akbarabadi, E. Barsotti, et al., Salt precipitation in ultratight porous media and its impact on pore connectivity and hydraulic conductivity, Water Resour. Res. 54 (4) (2018) 2768–2780, https://doi.org/10.1002/2017wr021194.
[25] L. Yan, Y. Chang, S.M. Hassanizadeh, et al., A quantitative study of salinity effect on water diffusion in n-alkane phases: from pore-scale experiments to molecular dynamic simulation, Fuel 324 (2022) 124716, https://doi.org/10.1016/j.fuel.2022.124716.
[26] N. Karadimitriou, S. Hassanizadeh, A review of micromodels and their use in two-phase flow studies, vzj2011.0072, Vadose Zone J. 11 (2012) 3, https://doi.org/10.2136/vzj2011.0072.
[27] S. Golmohammadi, Y. Ding, M. Kuechler, et al., Impact of wettability and gravity on fluid displacement and trapping in representative 2d micromodels of porous media (2d sand analogs), Water Resour. Res. 57 (10) (2021) e2021WR029908, https://doi.org/10.1029/2021WR029908.
[28] B. Zhao, C.W. MacMinn, R. Juanes, Wettability control on multiphase flow in patterned microfluidics, Proc. Natl. Acad. Sci. 113 (37) (2016) 10251–10256, https://doi.org/10.1073/pnas.1603387113.
[29] A. Kovscek, H. Wong, C. Radke, A pore-level scenario for the development of mixed wettability in oil reservoirs, AIChE J 39 (6) (1993) 1072–1085, https://doi.org/10.1002/aic.690390616.
[30] G. Mason, N.R. Morrow, Capillary behavior of a perfectly wetting liquid in irregular triangular tubes, J. Colloid Interface Sci. 141 (1) (1991) 262–274, https://doi.org/10.1016/0021-9797(91)90321-X.
[31] A. Mehmani, S. Kelly, C. Torres-Verdín, et al., Residual oil saturation following gas injection in sandstones: microfluidic quantification of the impact of pore-scale surface roughness, Fuel 251 (2019) 147–161, https://doi.org/10.1016/j.fuel.2019.02.118.
[32] R.T. Armstrong, S. Berg, Interfacial velocities and capillary pressure gradients during haines jumps, Phys. Rev. E 88 (4) (2013) 043010, https://doi.org/10.1103/PhysRevE.88.043010.
[33] R. Miri, R. van Noort, P. Aagaard, et al., New insights on the physics of salt precipitation during injection of CO_2 into saline aquifers, Int. J. Greenhouse Gas Control 43 (2015) 10–21, https://doi.org/10.1016/j.ijggc.2015.10.004.
[34] D. He, P. Jiang, R. Xu, Pore-scale experimental investigation of the effect of supercritical CO_2 injection rate and surface wettability on salt precipitation, Environ. Sci. Tech. 53 (24) (2019) 14744–14751, https://doi.org/10.1021/acs.est.9b03323.
[35] H.S. Rabbani, V. Joekar-Niasar, T. Pak, et al., New insights on the complex dynamics of two-phase flow in porous media under intermediate-wet conditions, Sci. Rep. 7 (1) (2017) 4584, https://doi.org/10.1038/s41598-017-04545-4.

[36] R. Hu, J. Wan, Z. Yang, et al., Wettability and flow rate impacts on immiscible displacement: a theoretical model, Geophys. Res. Lett. 45 (7) (2018) 3077–3086, https://doi.org/10.1002/2017GL076600.
[37] M. Kim, A. Sell, D. Sinton, Aquifer-on-a-chip: understanding pore-scale salt precipitation dynamics during CO_2 sequestration, Lab Chip 13 (13) (2013) 2508–2518, https://doi.org/10.1039/c3lc00031a.
[38] H. Salim, P. Kolpakov, D. Bonn, et al., Self-lifting NaCl crystals, J. Phys. Chem. Lett. 11 (17) (2020) 7388–7393, https://doi.org/10.1021/acs.jpclett.0c01871.
[39] W.Z. Yang, Y.S. Chang, J.D. Cheng, et al., Effects of pore structures on seepage and dispersion characteristics during CO_2 miscible displacements in unconsolidated cores, Energy Fuel 35 (21) (2021) 17791–17809, https://doi.org/10.1021/acs.energyfuels.1c02299.
[40] D.H. Kang, T.S. Yun, Minimized capillary end effect during CO_2 displacement in 2-d micromodel by manipulating capillary pressure at the outlet boundary in lattice boltzmann method, Water Resour. Res. 54 (2) (2018) 895–915, https://doi.org/10.1002/2017wr021409.
[41] X.S. Chen, R. Hu, C.X. Zhou, et al., Capillary-driven backflow during salt precipitation in a rough fracture, Water Resour. Res. 60 (3) (2024) e2023WR035451, https://doi.org/10.1029/2023WR03545.
[42] D. Zhang, Y. Kang, A. Selvadurai, et al., Experimental investigation of the effect of salt precipitation on the physical and mechanical properties of a tight sandstone, Rock Mech. Rock Eng. 53 (10) (2020) 4367–4380, https://doi.org/10.1007/s00603-019-02032-y.
[43] H. Zhang, Z. Sun, N. Zhang, et al., Brine drying and salt precipitation in porous media: a microfluidics study, Water Resour. Res. 60 (1) (2024) e2023WR035670, https://doi.org/10.1029/2023WR035670.
[44] Y. Liu, S. Berg, Y. Ju, et al., Systematic investigation of corner flow impact in forced imbibition, Water Resour. Res. 58 (10) (2022) e2022WR032402, https://doi.org/10.1029/2022WR032402.
[45] M. Aghajanloo, L. Yan, S. Berg, et al., Impact of CO_2 hydrates on injectivity during CO_2 storage in depleted gas fields: a literature review, Gas Sci. Eng. (2024) 205250, https://doi.org/10.1016/j.jgsce.2024.205250.
[46] R.R. Zhao, J.M. Cheng, Effects of temperature on salt precipitation due to formation dry-out during CO_2 injection in saline aquifers, Greenhouse Gas.-Sci. Technol. 7 (4) (2017) 624–636, https://doi.org/10.1002/ghg.1672.
[47] Y. Peysson, B. Bazin, C. Magnier et al., Permeability alteration due to salt precipitation driven by drying in the context of CO_2 injection, in: 10th International Conference on Greenhouse Gas Control Technologies, vol. 4, 2011, pp. 4387–4394. doi:10.1016/j.egypro.2011.02.391.
[48] A. Berntsen, J. Todorovic, M. Raphaug, et al., Salt clogging during supercritical CO_2 injection into a downscaled borehole model, Int. J. Greenhouse Gas Control 86 (2019) 201–210, https://doi.org/10.1016/j.ijggc.2019.04.009.
[49] M.A.M. Yusof, M.A. Ibrahim, M. Idress, et al., Effects of CO_2/rock/formation brine parameters on CO_2 injectivity for sequestration, SPE J. 26 (3) (2021) 1455–1468, https://doi.org/10.2118/203843-Pa.
[50] X. Hu, J. Wang, L. Zhang, et al., Direct visualization of nanoscale salt precipitation and dissolution dynamics during CO_2 injection, Energies 15 (24) (2022) 9567, https://doi.org/10.3390/en15249567.
[51] M. Kim, A. Sell, D. Sinton, Aquifer-on-a-chip: understanding pore-scale salt precipitation dynamics during CO_2 sequestration, Lab Chip 13 (13) (2013) 2508–2518, https://doi.org/10.1039/D4LC00296B.
[52] D. Akindipe, S. Saraji, M. Piri, Salt precipitation in carbonates during supercritical CO_2 injection: a pore-scale experimental investigation of the effects of wettability and heterogeneity, Int. J. Greenhouse Gas Control 121 (2022) 103790, https://doi.org/10.1016/j.ijggc.2022.103790.
[53] A. Tzachristas, D.G. Kanellopoulou, P.G. Koutsoukos, et al., The effect of surface wettability on calcium carbonate precipitation in packed beds, Surf. Interf. 34 (2022) 102354, https://doi.org/10.1016/j.surfin.2022.102354.